Microstructure and Dynamic Strain Aging Behavior in Oxide Dispersion Strengthened 91Fe-8Ni-1Zr (at.%) Alloy

Dallin J. Barton, Chaitanya Kale, B. Chad Hornbuckle, Kristopher A. Darling, Kiran N. Solanki, Gregory B. Thompson

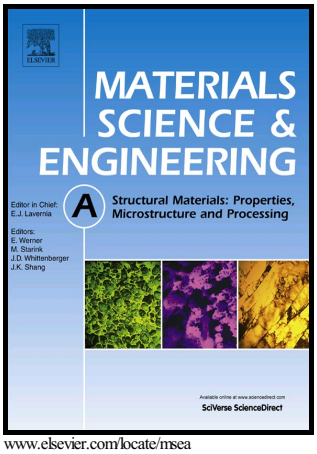

www.elsevier.com/locate/msea

PII: S0921-5093(18)30509-4
DOI: https://doi.org/10.1016/j.msea.2018.04.016
Reference: MSA36336

To appear in: *Materials Science & Engineering A*

Received date: 8 March 2018
Revised date: 3 April 2018
Accepted date: 4 April 2018

Cite this article as: Dallin J. Barton, Chaitanya Kale, B. Chad Hornbuckle, Kristopher A. Darling, Kiran N. Solanki and Gregory B. Thompson, Microstructure and Dynamic Strain Aging Behavior in Oxide Dispersion Strengthened 91Fe-8Ni-1Zr (at.%) Alloy, *Materials Science & Engineering A,* https://doi.org/10.1016/j.msea.2018.04.016

Microstructure and Dynamic Strain Aging Behavior in Oxide Dispersion Strengthened 91Fe-8Ni-1Zr (at.%) Alloy

Dallin J. Barton[1], Chaitanya Kale[2], B. Chad Hornbuckle[3], Kristopher A. Darling[3], Kiran N. Solanki[2], Gregory B. Thompson[1]

[1]University of Alabama, Department of Metallurgical & Materials Engineering, Box 870202 Tuscaloosa, AL 35487-0200 USA

[2]Arizona State University, School for Engineering of Matter, Transport, and Energy, Tempe, AZ 85287-0112 USA

[3]United States Army Research Laboratory, Weapons and Materials Research Directorate, Aberdeen Proving Grounds, Aberdeen, MD, 21005-5069 USA

Abstract

Mechanically alloyed 91Fe-8Ni-1Zr (at.%) powders were fabricated through high energy ball milling of elemental powder and subsequently consolidated via equal channel angular extrusion (ECAE) at 800°C and 1000°C. The resulting microstructure was fine grain with a nano-dispersion of Zr-oxide within the matrix, which was spherical for the 800°C. ECAE and plate-like (and volumetrically larger) for the 1000°C ECAE conditions. Atom probe tomography confirmed trace levels of C, N, and Cr impurities within the alloy making it similar to a low-carbon steel. By performing mechanical testing at a quasi-static strain rate (10^{-3} s^{-1}) and at high strain rate (10^{3} s^{-1}) at room temperature and 473 K, a load drop was noted after yielding. In general, this load drop became more pronounced with increasing strain rate and temperature and has been shown to be a result of dynamic strain aging in the ODS alloy.

Keywords: Atom probe tomography; ODS steel; High rate; Dynamic strain aging

1. Introduction

Oxide dispersion strengthened (ODS) materials such as ferrous-based alloys have been well conceived as potential applicants for next generation nuclear reactors because of their highly engineered nanometer-sized oxide particles within an Fe matrix. These oxide particles promote superior thermo-mechanical properties, such as high strength, creep and fatigue resistance [1,2]. In addition, these nano-oxide based alloys present exceptional radiation damage tolerance by providing an increase in the available interfacial surface area within the matrix that act as sinks for interstitials and vacancies; both of which can capture these byproducts in irradiation-based structural applications. Consequently these properties have attracted considerable attention for the nuclear energy industry as fuel cell claddings for next generation fission power plants [3,4].

To achieve the tailored mechanical behavior, research in the past has been focused on processing Fe-based alloys containing Y and/or Y-Ti- based nanosized dispersions [5,6]. Non-equilibrium processing techniques involving appropriate additions of Y and Ti as solutes results in formation of coherent, complex-oxides with sizes ranging up to a few nanometers which are distributed within the Fe matrix. In addition, Cr has been added as a means to increase corrosion resistance while at the same time microstructural stability by preventing the BCC-to-FCC phase transformations at elevated temperatures. Such ODS alloys have been proven to be extremely stable and effective when tested under the extreme environments [2].

Recently, Darling et al. have suggested that additions of Zr could provide an alternative to mechanically alloyed Y_2O_3 and Ti-solute based nanostructured ferritic ODS alloys [7]. Just like Y and Ti, Zr readily reacts with oxygen to form a dispersion of these nano-scale ZrO_2-based particles. These ZrO_2-based particles can have a similar degree of coherency with the matrix as with the more common Y_2O_3 based oxides [8,9] and can also act as a potent grain-size stabilizing agent [7]. Furthermore, Kotan et al. [10,11] in conjunction with Darling et al. [12], proposed a simple ternary nanostructured ODS alloy with a composition of (92-X)-Fe-8Ni-(X)Zr, where X = 1 to 4 at. %. With the addition of 8 at% Ni, the BCC-to-FCC phase transformation temperature was lowered to ~ 673 K [10,11]. At these lower temperatures, diffusion becomes sluggish and the kinetics for the phase transformation can then be use to tune the microstructure. For instance, the phase transformation instability allows for easier bulk consolidation via equal channel angular extrusion (ECAE) because of the more formable FCC phase [7]. Likewise the phase transformation can used to design a bimodal grain size microstructure [13] and such microstructures has been ascribed as a method to increase ductility while maintaining strength

especially in nanocrystalline alloys. The kinetics of any abnormal grain growth observed in these alloys have been shown to depend on temperature and Zr concentration, where high Zr compositions lead to precipitation of secondary phase intermetallics/oxides, which influence the rate of phase boundary expansion during the BCC-to-FCC transformation [10]. Thus the phase transformation, along with the nano-scale ZrO_2-based particles, can be viewed as a method by which new ODS alloys can be designed and created having applications spanning beyond those of just the nuclear industry, including transportation and space shielding applications.

To that end, the strain rate effects in a 91Fe-8Ni-1Zr (at.%) based ODS alloy are measured and reported in this paper. To achieve this, quasi-static (10^{-3} s^{-1}) and high strain rate (10^{3} s^{-1}) compression experiments were performed at room temperature (298 K) and 473 K. To the authors' knowledge, the study of ODS materials under high strain rate has yet to be reported or understood. While literature has shown that grain size and particle dispersions dictate the strength in ODS alloys, their contribution to higher strain-rate deformation behavior has been not elucidated in these ODS alloys. This would provide new insights into the underlying deformation mechanisms under such conditions.

2. Experimental Procedure

2.1 Material Synthesis

The 91Fe-8Ni-1Zr (at.%) alloy was fabricated by mechanical alloying via high energy ball milling the requisite elemental powder blend [12] in a SPEX 8000D shaker mill. The 99.9% Fe, 99.8% Ni, and 99.5% Zr virgin powders (Alfa Aesar, Ward Hill, MA) were sieved via a 325 mesh and loaded into steel vials (SPEX model 8007) inside a glove box with an Ar atmosphere (< 1ppm oxygen). A series of 440C stainless steel balls were used for milling with a ball-to-powder ratio of 10-to-1 by weight. After milling, the powders were stored in the aforementioned glove box until roughly 100 grams of powder were generated for consolidation. Samples were consolidated in Ni cans at 800°C and 1000°C using a $4B_c$ ECAE processing route [14]. During ECAE processing, the residual oxygen is sufficient to oxidize the Zr and precipitate out the nanoscale oxide dispersion. The final consolidate material was dense, less than 2% porous.

2.2 Characterization

After ECAE processing, the consolidated samples' grain size was quantified using the line intercept method from ion contrast images taken on a FEI Nova dual electron – focus ion beam (FIB) microscope. Phase was determined by X-ray diffraction (XRD) on a Co-source Bruker D8 Discover with GADDS and electron backscattered diffraction (EBSD) on a Tescan Lyra microscope operated at 20 keV using an EDAX TEAM platform. The same samples' oxide dispersions were quantified for size, inter-particle spacing, and composition by atom probe tomography (APT) in the post-mechanical tested condition. The atom probe samples were lifted out and annular milled into the required needle-like specimen shape using an FEI Quanta Dual Beam and Lyra Tescan FIBs for the post-mechanical tested conditions. Details of the procedure can be found in reference [15]. With the tips prepared, they were field evaporated in a Cameca Local Electrode Atom Probe (LEAP) 5000XS with all samples run in the laser mode. Various laser energies and temperatures were explored to obtain the optimal run parameters. These were found to be with a laser energy of 100 pJ with the tip at an operating temperature of 40 K. The pulse frequency was set between 300-600 kHz with detection rates between 0.5-1.0%. The data sets were then analyzed with Cameca's Interactive Visualization and Analysis Software (IVAS 3.6.14 and IVAS 3.8) platform with the reconstruction done in the shank angle mode.

2.3 Mechanical Testing

Room temperature uniaxial tensile tests were performed at a quasi-static (10^{-3} s^{-1}) strain rate using dog-bone samples, which were ECAE processed at 1000°C. Similarly, cylindrical compression samples with a 3 mm height and 3 mm diameter were cut from each of the 800°C and 1000°C ECAE processed materials. Compression testing was performed at quasi-static (10^{-3} s^{-1}) and high-rate ($4x10^{3}$ s^{-1}) at room temperature (298 K) and 473 K, with the temperature provided by a furnace that encapsulated the specimen and the major testing parts of each apparatus. In both cases, the system was held at the testing temperature for about 30 minutes to attain thermal equilibrium, with a thermocouple attached on the specimen to monitor the temperature. Quasi-static uniaxial compression and compression loading-unloading tests were performed on an INSTRON load frame with a 50 kN load capacity while high rate experiments were performed on a 12.7 mm Inconel Kolsky bar [16,17] apparatus. Further details of the Kolsky bar test method can be found in [18].

3. Results and Discussion

3.1 Material Microstructure

The ECAE consolidated samples at 800°C and 1000°C had grain sizes of 1 ± 0.5 μm and 4 ± 0.5 μm, respectively, shown in Figure 1. EBSD and XRD confirmed the BCC phase and these results are similar to references [10] and [12]. The compositional analysis of the alloy, via APT, was found to be more challenging because of specific isotope and charge state overlaps as well as numerous complex ion evaporation events. In the supplementary section of this paper, the full mass spectrum is provided in Figure S.1 that identifies the specific species to their mass-to-charge ratios.

While the statistical availability of isotopes, in general, can help in the decomposition of such peaks, this is most accurate when the tips are field evaporated in the voltage mode. In the laser mode, which provides thermal assistance to field evaporation, the oxide isotope values, for example, can vary depending on laser power which makes any such decomposition difficult to decipher [19]. However, in order to successfully field evaporate these alloys with their nano-oxides, the laser assisted field evaporation was required. Attempts using voltage pulsing was found to be unsuccessful in yielding large data sets sufficient for analysis. Thus, care should be used in interpreting the full composition laser assisted evaporation because of the aforementioned concerns. Nevertheless, even with these issues, the overall composition listed in Table 1, was very near that of starting powder mixtures, giving confidence in the presented results.

To identify the oxide dispersions in the 91Fe-8Ni-1Zr/800°C ECAE sample, we implemented the nearest neighbor and maximum separation cluster analysis [20–22] available in IVAS whereupon the size, concentration, and distance from each other was found, Figure 2(a). The number density of the clusters/particles was 2.48E23 m^{-3} and the Delaunay tessellation derived interparticle spacing [23] was, on average, 24 nm with a minimum spacing of 1 nm and a maximum spacing of 141 nm via the cluster analysis technique. Using the identified clusters/particles, isoconcentration surfaces or isosurfaces were generated around these features, Figure 2(b), and the proximity histogram (proxigram) was created, Figure 2(c)-(d), using the procedure reported by Hornbuckle et al. [24]. The two proxigrams, Figure 2(c) and (d), are given because of the relative absolute values (y-axis) of the species identified. Interestingly, Cr was found to enrich the interface of the oxide particles, Figure 2(d). Unlike some other ODS systems, such as YWT, Cr has not been reported to segregate to the interface but rather be retained at a

higher composition within the matrix or inside the particle [25] which may be contributed to the different type of oxide formed here.

Using a similar approach for the 91Fe-8Ni-1Zr/1000°C ECAE sample, the clusters, isosurfaces, and their corresponding proxigrams are shown in Figure 3(a)-(d). Here, the cluster/particle density was found to be 2.42E23 m^{-3} and the average interparticle spacing was 43 nm with a range of 2 nm to 426 nm using the cluster analysis. Two items of note were identified. First, the isosurface values were different between the two samples, i.e. 8 at% Zr for the 800°C ECAE sample and 10 at.% for the 1000°C ECAE sample. The identification of this particular iso-value is determined by the inflection point of the decomposed Zr ions between the matrix and particle [24]. The shift in this value indicates that the oxide particles have compositionally evolved between the two ECAE processes. In particular, we observed a smaller gradient change in the Ni content and less of a nitrogen increase in the particles with the elevated processing temperature (Figure 2(d) vs. Figure 3(d)). The second feature was that the identified clusters/particles appeared more elongated, plate-like in morphology with the increased ECAE temperature (Figure 2(a) vs. Figure 3(a)). This change in shape suggest more flow-ability of the material at the higher thermo-mechanical extrusion conditions, which could be expected. Furthermore, the mean volume computed for the 800°C ECAE was 99 nm^3 with a range between 3.9 nm^3 and 3.1E3 nm^3. Upon increasing the ECAE temperature to 1000°C, the mean volume of the oxide dispersion was found to be 444 nm^3 with a range of 7.5 nm^3 to 14.5E4 nm^3, which again would be expected with the higher temperatures increasing the diffusivity distances of the solutes to react, precipitate, and grow.

The composition of both the matrix and particles are tabulated in Table 1. Here, an isolated cylinder region of interest was drawn within each separate phase (matrix vs. oxide particle) with the mass spectrum taken from that region. Reviewing Table 1, we note, and as expected, the Zr solute segregated into particles with increases in C, N, O, H, and Cr levels as compared to the matrix because of its higher affinity to these species. Though C, N, and O were not intentionally added during fabrication, they are intrinsic to starting the powders with Alfa Aeasar reporting levels of 0.13% C, 0.3% O, and 0.008% N. In addition, these elements as well as Cr, could be incorporated through the subsequent ball-milling process and/or reactions with the atmosphere during processing. Upon closer inspection of Table 1 and the proxigrams of Figures 1 and 2, the Zr content appears to be ~ 35 at% and oxygen being ~ 53 at.%, with the

balance being mainly N and Fe. The variation in these compositions from the expected ZrO_2 stoichiometry is attributed to the complex and preferential field evaporation events from zirconia, which has been previously reported in [26].

From the microstructural characterization, the following conclusions are drawn: (1) The increasing ECAE processing temperature results in an expected grain growth. (2) The presence of intrinsic impurities, including oxygen, facilitate the precipitation of nano-dispersion of Zr-oxides within the matrix. (3) The carbon and nitrogen showed a preference to partition to these Zr-based oxide particles. And (4) upon higher ECAE temperatures, these spherical precipitates' morphology evolved into a more plate-like shape with the mean volume increasing and number density and inter-particle spacing being relatively invariant to the changes for the ECAE temperatures studied. This suggests that the increased ECAE temperature promotes both new precipitation and growth with increasing temperature.

3.2 Mechanical Properties

Each of the samples was mechanically tested in compression and tension at room temperature (RT, 298 K) and 473 K at a strain rates of 0.001 s^{-1} (quasi-static) and $4x10^3$ s^{-1} (high-rate), with the corresponding curves shown in Figure 4. In the quasi-static condition, the RT yield strength were 1690 MPa and 1436 MPa for the 800°C and 1000°C ECAE conditions respectively. Since the number density (2.42E23 m^{-3} vs 2.48E23 m^{-3}) is nearly equivalent between the two conditions, this modest decrease in the yield strength is mostly likely contributed to the increase in grain size (1 ± 0.5 μm vs. 4 ± 0.5 μm) between the two samples as associated with the Hall-Petch effect. Upon closer inspection of the compression tested quasi-static curves (dashed curves), inset image in Figure 4(a), a slight load drop was observed that becomes even more pronounced in the high strain rate compression tests (solid lines), Figure 4(b). In addition, the 800°C ECAE sample's highest strain rate revealed a notable increase in the yield point to 1895 MPa which was not as evident for the 1000°C ECAE sample. In comparison, the loading curves at 473 K revealed the absence of the aforementioned modest load drop at the quasi-static conditions; however, the very distinctive load drop was retained in the high strain rate compression conditions, Figures 4(c) and (d). The increase in the yield point, with strain rate, is now readily apparent in both curves tested at 473 K. Interestingly, a serrated flow pattern is observed in the high strain-rate for the 1000°C ECAE/473 K sample, but this is likely an artifact

of resonance ringing effects during the Hopkinson-Kolsky test [27]. The collection of the mechanical values from these tests are tabulated in Table 2.

To further investigate the rate dependent load drop, the 1000°C ECAE samples, now tested in compression at RT, were loaded at 0.001 s^{-1}, 0.01 s^{-1}, and 0.1 s^{-1} with the data plotted in Figure 5. As the strain rate increased, an ever apparent drop of a few MPa's is recorded with the increased rate. It is apparent that the load drop is indeed linked to the strain rate in the compression testing.

The mechanical strengthening of ODS alloys have long been associated with the nano-scale oxide dispersions. Orowan strengthening is considered one of the very common methods of strengthening in ODS alloys [28], Though the increase in strength with straining can be linked to this mechanism, the presence of this load drop is likely not related to the Orowan strengthening mechanism. Rather the dislodgment of dislocations from a Cottrell atmosphere, a phenomenon commonly observed in strain-aged mild steels, would be more probable. A Cottrell atmosphere is found when impurities distort the surrounding lattice slightly creating a stress field that is relaxed by eventually have the solutes migrate to a dislocation [29]. Recent simulation studies have shown the interaction of dislocation core with the solute atoms in Fe [30,31]. When the impurities congregate together, they act as particles that then impede dislocation motion. Dynamic strain aging occurs when these dislocations are then liberated from their partitioned solutes that reside in their cores. As these dislocations become free from the solutes that pin them, the corresponding stress is reduced, and a load drop is observed. The initial load drop is the most severe because the dislocation cores are initially partitioned with the highest solute concentrations with subsequent flow stress not having the same level of solute partitioning [32,33]. This phenomenon is commonly seen in low carbon (and nitrogen) containing steels [34]. Based upon the APT compositional analysis in Table 1, trace impurities of C and N are within the matrix and this ferrous alloy would make it classified as a low carbon steel. In Figure 5, it is clear as the strain rate increases, the load drop increases, which would be in agreement for a condition that more readily moves the dislocations faster from the solute atmosphere.

In order to determine if dynamic strain aging is indeed responsible, another series of mechanical tests were performed to test this hypothesis. A quasi-static compression test was performed on the 1000°C ECAE sample, at RT, shown in Figure 6(a). Upon the initial compression testing, at a quasi-static rate of 0.001 s^{-1}, a load drop is observed. By immediately

reloading at RT, the solutes have not had (or had a very limited) opportunity to diffuse back to the dislocation cores. The diffusion rates of C and N in Fe at RT is ~5E-19 cm^2s^{-1} [35] and ~2E-16 cm^2s^{-1} [36] respectively. As hypothesized, there is not an obvious load drop after immediate re-testing, Figure 6(a). Upon letting the sample age at RT for 340 hours and 670 hours, again no strongly evident load drop, as compared to the 'initial' loading curve, is observed, confirming the slow diffusivity in the alloy and such results are consistent with the findings of Seal [37]. Upon annealing the same sample at 673 K for two hours, sufficient thermal energy is now present to promote the C and N diffusion back to the dislocation cores. At 673 K, the C and N diffusivity rates are 3E-11 cm^2s^{-1} [35] and 6E-9 cm^2s^{-1} [36] respectively. Reloading the sample at the same compressive loading conditions as the initial test reveals a return of the load drop, Figure 6(a). This provides the clearest evidence that dynamic strain aging is occurring within these ODS materials. Though this does not necessarily eliminate other potential deformation mechanisms that may be active during these tests, dynamic strain aging is likely the most significant.

Finally, the 1000°C ECAE sample was again aged at 400°C but now tested in tension under the quasi-static (0.001 s^{-1}) rate, shown in Figure 6(b). Again, the load drop is noted to occur as well as a serrated flow with continued straining. This serrated flow is associated with the Portevin-Le Chatlier effect, which is revealed under tensile conditions, is again a classic response seen in dynamic strain aged mild steels providing further confirmation of this mechanism.

Conclusion

A mechanically alloyed 91Fe-8Ni-1Zr (at.%) powder was fabricated through high energy ball milling and subsequently consolidated via ECAE processing either at 800°C or 1000°C. The different temperatures resulted in an average grain growth from 1 μm to 4 μm, which corresponded to a modest yield point reduction associated with the Hall-Petch effect. APT characterization revealed nano-sized zirconium oxide dispersions within the material, with the morphology being more spherical at 800°C ECAE and more plate-like at 1000°C ECAE. The increased ECAE temperature also promoted the increase in the mean volume of the oxides from ~ 99 nm^3 to ~ 444 nm^3. The number density (~2.4 x 10^{23} m^{-3}) and interparticle spacing (~25 to ~40 nm) did not significantly change with the increase in ECAE temperature.

Quasi-static and high rate strain testing, in tension and compression, revealed a load drop upon yielding, with the extent of the drop becoming more pronounced with increasing strain rate. Upon closer evaluation of the APT compositional data, the presence of C and N was noted at levels that make the ODS material similar to other low C and N containing steels suggesting that the load drop is a result of dynamic strain aging. To prove this, a secondary quasi-static compression test was performed. The sample was loaded to a certain strain level, unloaded and immediately loaded again. The first load showed a load drop. The reload showed no drop. The same sample was aged at RT for 670 hours and loaded again with no load drop. Upon heating at 673 K for two hours, a load drop reappeared. Further confirmation of the dynamic strain aging was also observed by serrated flow associated with the Portevin-Le Chatlier effect when the same sample was tested in tension at RT.

Though ODS materials can be produced by intrinsic oxidation reactions with associated high affinity metals, other trace impurities, particularly C and N, within the Fe matrix can segregate to dislocation cores creating conditions whereupon dynamic strain aging effects can become more prevalent under high strain-rate mechanical loading. While grain size and particle dispersions are known to dictate the strength in ODS alloys, this work suggests that the partition of trace impurities to dislocations is more significant in altering the active deformation response, especially within the higher strain rate regimes. To the authors' knowledge, this has been the first series of high-rate testing revealing dynamic strain aging effects in ODS materials.

Acknowledgment:

The authors gratefully acknowledge ARO-W911NF-15-2-0050 for supporting this research. C. Kale and K.N. Solanki acknowledge the financial support for this work from the Army Research Laboratory award number W911NF-15-2-0038.

References

[1] S. Ukai, H. Okada, M. Inoue, T. Nishida, M. Fujiwara, S. Nomura, S. Shikakura, K. Asabe, Alloying design of oxide dispersion for long life FBRs core materials strengthened ferritic steel, J. Nucl. Mater. 204 (1993) 5–73.

[2] C.H. Zhang, Y.T. Yang, Y. Song, J. Chen, L.Q. Zhang, J. Jang, A. Kimura, Irradiation response of ODS ferritic steels to high-energy Ne ions at HIRFL, J. Nucl. Mater. (2014). doi:10.1016/j.jnucmat.2014.04.015.

[3] S. Ukai, S. Mizuta, M. Fujiwara, T. Okuda, T. Kobayashi, Development of 9Cr-ODS Martensitic Steel Claddings for Fuel Pins by means of Ferrite to Austenite Phase

Transformation, J. Nucl. Sci. Technol. 39 (2002) 778–788. doi:10.1080/18811248.2002.9715260.
[4] B.J. Lewis, W.T. Thompson, F. Akbari, C. Morrison, A. Husain, Thermodynamic considerations and prediction of the primary coolant activity of 99Tc, J. Nucl. Mater. (2005). doi:10.1016/j.jnucmat.2004.10.116.
[5] M.K. Miller, K.F. Russell, H. D.T., Characterization of Precipitates in MA/ODS ferritic alloys., J. Nucl. Mater. 351 (2006) 261–268. doi:10.1016/j.actamat.2012.12.042.
[6] L. Hsiung, M. Fluss, S. Tumey, J. Kuntz, B. El-Dasher, M. Wall, B. Choi, A. Kimura, F. Willaime, Y. Serruys, HRTEM study of oxide nanoparticles in K3-ODS ferritic steel developed for radiation tolerance, (2011). doi:10.1016/j.jnucmat.2010.09.014.
[7] Y.-J. Hu, J. Li, K.A. Darling, W.Y. Wang, B.K. Vanleeuwen, X.L. Liu, L.J. Kecskes, E.C. Dickey, Z.-K. Liu, Nano-sized Superlattice Clusters Created by Oxygen Ordering in Mechanically Alloyed Fe Alloys, (2015). doi:10.1038/srep11772.
[8] L.L. Hsiung, M.J. Fluss, A. Kimura, Structure of oxide nanoparticles in Fe-16Cr MA/ODS ferritic steel, Mater. Lett. 64 (2010) 1782–1785. doi:10.1016/j.matlet.2010.05.039.
[9] P. Dou, A. Kimura, R. Kasada, T. Okuda, M. Inoue, S. Ukai, S. Ohnuki, T. Fujisawa, F. Abe, S. Jiang, Z. Yang, TEM and HRTEM study of oxide particles in an Al-alloyed high-Cr oxide dispersion strengthened steel with Zr addition, J. Nucl. Mater. 444 (2014) 441–453. doi:10.1016/j.jnucmat.2013.10.028.
[10] H. Kotan, K.A. Darling, M. Saber, R.O. Scattergood, C.C. Koch, Thermal stability and mechanical properties of nanocrystalline Fe-Ni-Zr alloys prepared by mechanical alloying, J. Mater. Sci. 48 (2013) 8402–8411. doi:10.1007/s10853-013-7652-7.
[11] H. Kotan, K.A. Darling, M. Saber, R.O. Scattergood, C.C. Koch, An in situ experimental study of grain growth in a nanocrystalline Fe91Ni8Zr1 alloy, J. Mater. Sci. 48 (2013) 2251–2257. doi:10.1007/s10853-012-7002-1.
[12] K.A. Darling, M. Kapoor, H. Kotan, B.C. Hornbuckle, S.D. Walck, G.B. Thompson, M.A. Tschopp, L.J. Kecskes, Structure and mechanical properties of Fe-Ni-Zr oxide-dispersion-strengthened (ODS) alloys, J. Nucl. Mater. (2015). doi:10.1016/j.jnucmat.2015.09.011.
[13] L. Huang, W. Lin, B. Lin, F. Liu, Exploring the concurrence of phase transition and grain growth in nanostructured alloy, Acta Mater. 118 (2016) 306–316. doi:10.1016/j.actamat.2016.07.052.
[14] R.Z. Valiev, T.G. Langdon, Principles of equal-channel angular pressing as a processing tool for grain refinement, Prog. Mater. Sci. 51 (2006) 881–981. doi:10.1016/j.pmatsci.2006.02.003.
[15] G.B. Thompson, L. Wan, X. xiang Yu, F. Vogel, Influence of phase stability on the in situ growth stresses in Cu/Nb multilayered films, Acta Mater. 132 (2017) 149–161. doi:10.1016/j.actamat.2017.04.036.
[16] B. Hopkinson, A Method of Measuring the Pressure Produced in the Detonation of High Explosives or by the Impact of Bullets, Philos. Trans. R. Soc. London. 213 (1914) 437–456.
[17] H. Kolsky, An Investigation of the Mechanical Properties of Materials at very High Rates of Loading, Proc. Phys. Soc. Lond. B. 62 (1949) 676–700.
[18] C. Kale, M. Rajagopalan, S. Turnage, B. Hornbuckle, K. Darling, S. Mathaudhu, K. Solanki, On the roles of stress-triaxiality and strain-rate on the deformation behavior of AZ31 magnesium alloys, Mater. Res. Lett. 6 (2018) 152–158.
[19] R. Kirchhofer, M.C. Teague, B.P. Gorman, Thermal effects on mass and spatial resolution

during laser pulse atom probe tomography of cerium oxide, J. Nucl. Mater. 436 (2013) 23–28. doi:10.1016/j.jnucmat.2012.12.052.
[20] S. Rogozhkin, A. Bogachev, O. Korchuganova, A. Nikitin, N. Orlov, A. Aleev, A. Zaluzhnyi, M. Kozodaev, T. Kulevoy, B. Chalykh, R. Lindau, J. Hoffmann, A. Möslang, P. Vladimirov, M. Klimenkov, M. Heilmaier, J. Wagner, S. Seils, Nanostructure evolution in ODS steels under ion irradiation, Nucl. Mater. Energy. 14 (2016) 1–9. doi:10.1016/j.nme.2016.06.011.
[21] C.A. Williams, D. Haley, E.A. Marquis, G.D.W. Smith, M.P. Moody, Defining clusters in APT reconstructions of ODS steels, Ultramicroscopy. 132 (2013) 271–278. doi:10.1016/j.ultramic.2012.12.011.
[22] B. Gault, M.P. Moody, J.M. Cairney, S.P. Ringer, Atom Probe Microscopy, 1st ed., Springer, 2012.
[23] W. Lefebvre, T. Philippe, F. Vurpillot, Application of Delaunay tessellation for the characterization of solute-rich clusters in atom probe tomography, Ultramicroscopy. 111 (2011) 200–206. doi:10.1016/j.ultramic.2010.11.034.
[24] B.C. Hornbuckle, M. Kapoor, G.B. Thompson, A procedure to create isoconcentration surfaces in low-chemical-partitioning, high-solute alloys, Ultramicroscopy. 159 (2015) 346–353. doi:10.1016/j.ultramic.2015.03.003.
[25] M. Brocq, B. Radiguet, S. Poissonnet, F. Cuvilly, P. Pareige, F. Legendre, Nanoscale characterization and formation mechanism of nanoclusters in an ODS steel elaborated by reactive-inspired ball-milling and annealing, J. Nucl. Mater. 409 (2011) 80–85. doi:10.1016/j.jnucmat.2010.09.011.
[26] Y.M. Chen, T. Ohkubo, M. Kodzuka, K. Morita, K. Hono, Laser-assisted atom probe analysis of zirconia/spinel nanocomposite ceramics, Scr. Mater. 61 (2009) 693–696. doi:10.1016/j.scriptamat.2009.05.043.
[27] B. Song, E. Nishida, B. Sanborn, M. Maguire, D. Adams, J. Carroll, J. Wise, B. Reedlunn, J. Bishop, T. Palmer, Compressive and Tensile Stress–Strain Responses of Additively Manufactured (AM) 304L Stainless Steel at High Strain Rates, J. Dyn. Behav. Mater. 3 (2017) 412–425. doi:10.1007/s40870-017-0122-6.
[28] L. Li, W. Xu, M. Saber, Y. Zhu, C.C. Koch, R.O. Scattergood, A Long-term stability of 14YT – 4Sc alloy at high temperature, Mater. Sci. Eng. A. 647 (2015) 222–228. doi:10.1016/j.msea.2015.09.012.
[29] A.H. Cottrell, B.A. Bilby, Dislocation Theory of Yielding and Strain Ageing of Iron, Proc. Phys. Soc. Sect. A. 62 (1949) 49. doi:10.1088/0370-1298/62/1/308.
[30] L. Ventelon, B. Lüthi, E. Clouet, L. Proville, B. Legrand, D. Rodney, F. Willaime, Dislocation core reconstruction induced by carbon segregation in bcc iron, Phys. Rev. B. 91 (2015) 220102.
[31] M.A. Bhatia, S. Groh, K.N. Solanki, Atomic-scale investigation of point defects and hydrogen-solute atmospheres on the edge dislocation mobility in alpha iron, J. Appl. Phys. 116 (2014) 64302. doi:10.1063/1.4892630.
[32] G.E. Dieter, Mechanical Metallurgy, McGraw-Hill, London, 1988. doi:0-07-100406-8.
[33] A.. Cottrell, LXXXVI. A Note on the Portevin-Le Ghatelier Effect By A. H., 44 (1952) 829–832.
[34] M.J. Hadianfard, R. Smerd, S. Winkler, M. Worswick, Effects of strain rate on mechanical properties and failure mechanism of structural Al – Mg alloys, 492 (2008) 283–292. doi:10.1016/j.msea.2008.03.037.

[35] A. J, Tracer diffusion data for metals, alloys and simple oxides., Plenum Publishing Corporation, New York City, 1970.
[36] T.C. Totemeier, G. W.F., Smithells Metals Reference Book, 8th ed., Elsevier Butterworth-Heinemann Publications, The Netherlands, 2004.
[37] R.K. Seal, New Ultra-Low Carbon High Strength Steels with Improved Bake Hardenability for Enhanced Stretch Formability and Dent Resistance, University of Pittsburgh, 2006.

Fig 1: The ion contrast image of the ECAE 800^{o}C and 1000^{o}C ODS samples.

Fig 2: 91Fe-8Ni-1Zr ECAE processed at 800°C. **(a)** A nearest neighbor cluster analysis with the visualization of the identified clusters/particles **(b)** An ion map with 8 at.% (confidence σ-3) decomposed Zr isosurface for comparison. The 8 at.% Zr isosurfaces were used to determine the proxigrams listed in **(c)** and **(d)**.

Fig 3: 91Fe-8Ni-1Zr ECAE processed at 1000°C. **(a)** A nearest neighbor cluster analysis with the visualization of the identified clusters/particles **(b)** An ion map with 10 at.% (confidence σ-3) decomposed Zr isosurface for comparison. The 10 at.% Zr isosurfaces were used to determine the proxigrams listed in **(c)** and **(d)**.

Fig 4: High-rate and quasi-static tests of 91Fe-8Ni-1Zr in compression. **(a)** ECAE processed at 800°C and tested at room temperature. **(b)** ECAE processed at 1000°C and tested at room temperature. **(c)** ECAE processed at 800°C and tested at 473 K **(d)** ECAE processed at 1000°C and tested at 473 K

Fig 5: Compression tests at different quasi-static strain rates performed on 91Fe-8Ni-1Zr ECAE processed at 1000°C at room temperature. The drop in the load post yielding is directly related to the strain rate tested.

Fig 6: 91Fe8Ni1Zr ECAE processed at 1000°C. **(a)** Quasi-static compression tested at room temperature (298 K). After the initial load, a second load was placed immediately afterwards. The load drop disappeared. After waiting at room temperature for 340 and 670 hours, the sample did not exhibit a load drop again. The sample was then aged at 673 K for 2 hours and tested again at RT. The load drop reappeared demonstrating the dynamic strain aging mechanism. **(b)** Tensile testing at the quasi-static condition (10^{-3} s^{-1}) revealing the load drop as well as the Portevin-Le Chatlier effect.

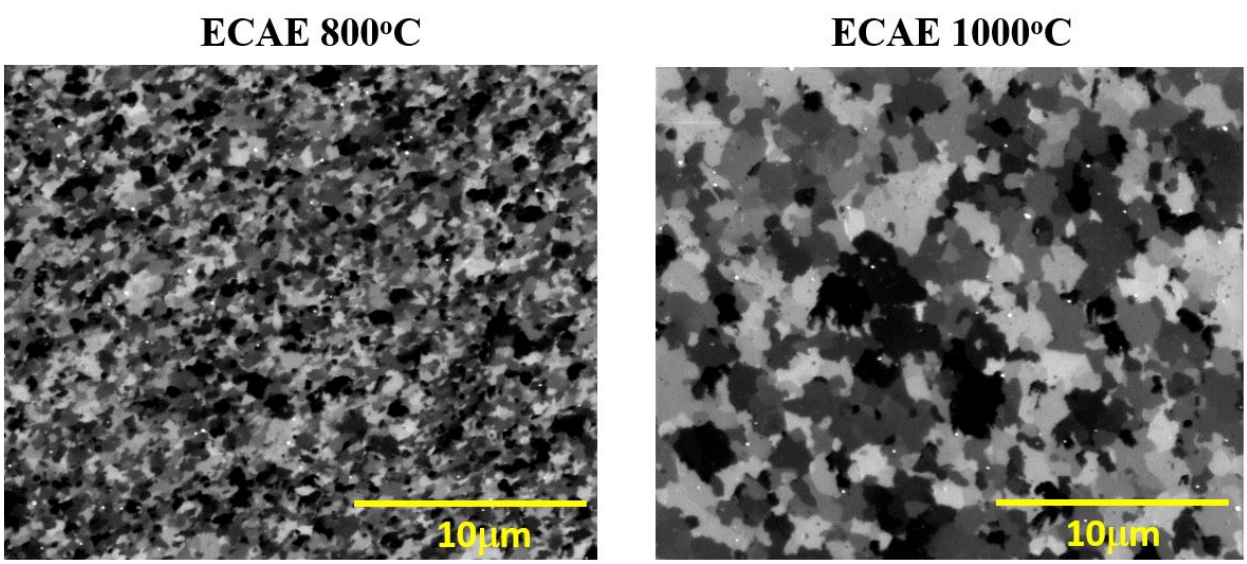

Fig. 1

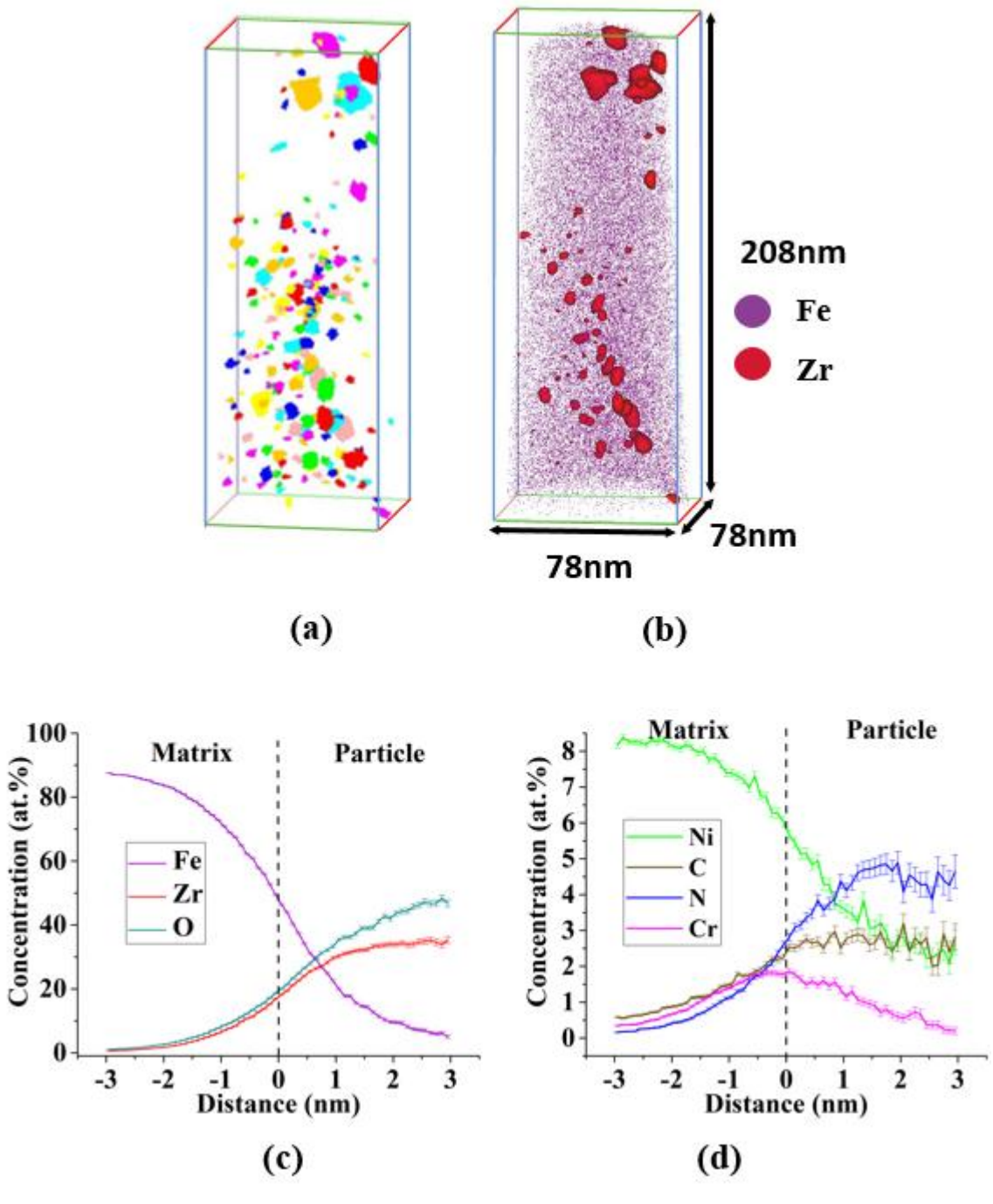
208nm
Fe
Zr
78nm
78nm
(a)
(b)
Matrix
Particle
Concentration (at.%)
Fe
Zr
O
Distance (nm)
(c)
Matrix
Particle
Concentration (at.%)
Ni
C
N
Cr
Distance (nm)
(d)

Fig. 2

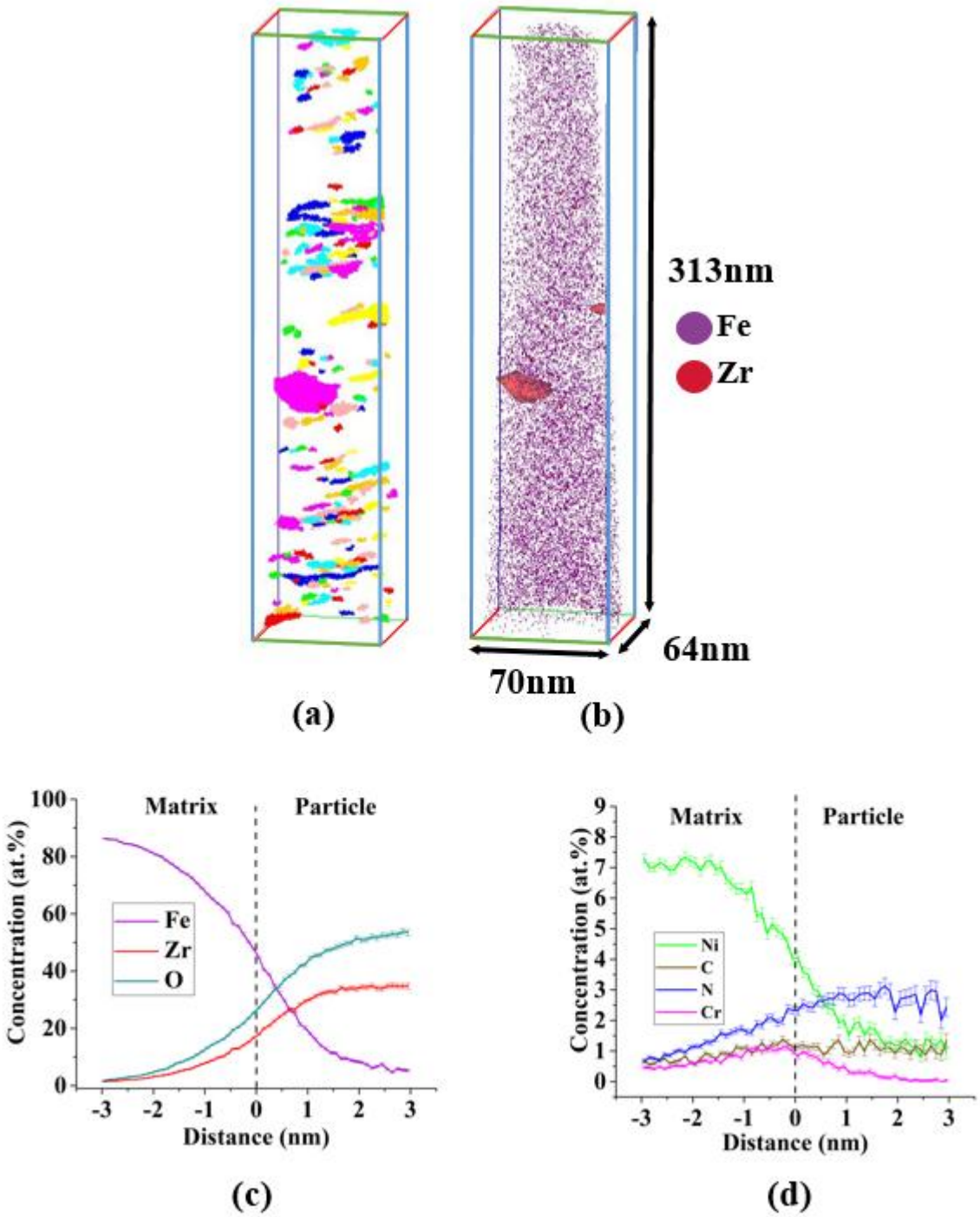
313nm
Fe
Zr
64nm
70nm
(a)
(b)
Matrix
Particle
Concentration (at.%)
Fe
Zr
O
Distance (nm)
(c)
Matrix
Particle
Concentration (at.%)
Ni
C
N
Cr
Distance (nm)
(d)

Fig. 3

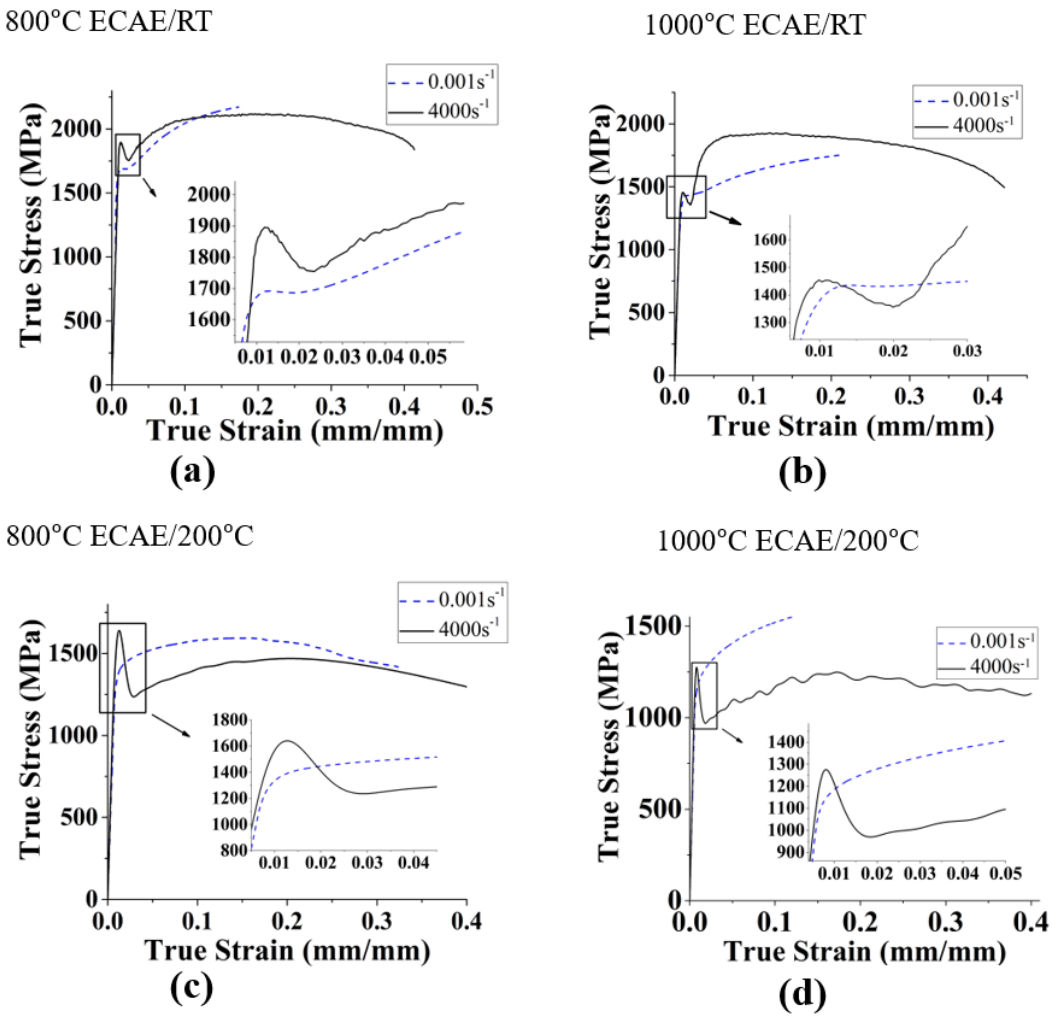
800°C ECAE/RT
0.001s-1
4000s-1
True Stress (MPa)
True Strain (mm/mm)
(a)
1000°C ECAE/RT
0.001s-1
4000s-1
True Stress (MPa)
True Strain (mm/mm)
(b)
800°C ECAE/200°C
0.001s-1
4000s-1
True Stress (MPa)
True Strain (mm/mm)
(c)
1000°C ECAE/200°C
0.001s-1
4000s-1
True Stress (MPa)
True Strain (mm/mm)
(d)

Fig. 4

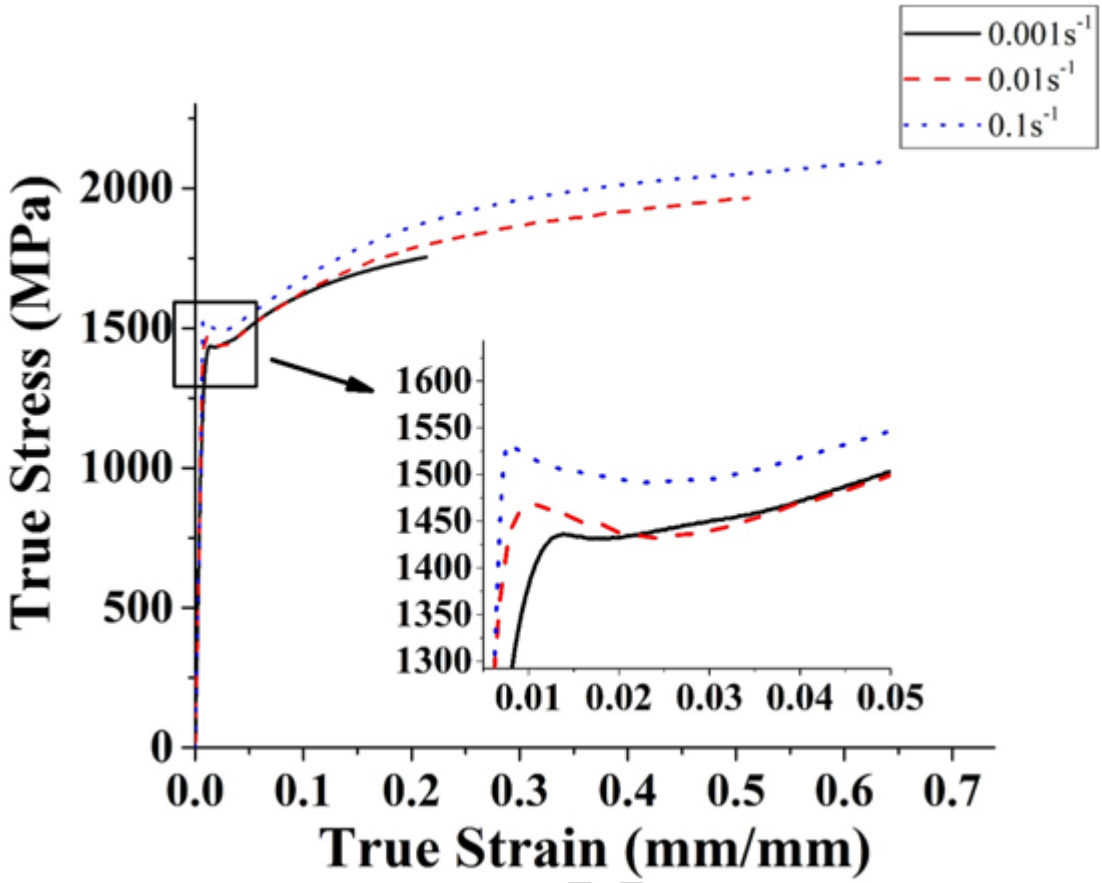

Fig. 5

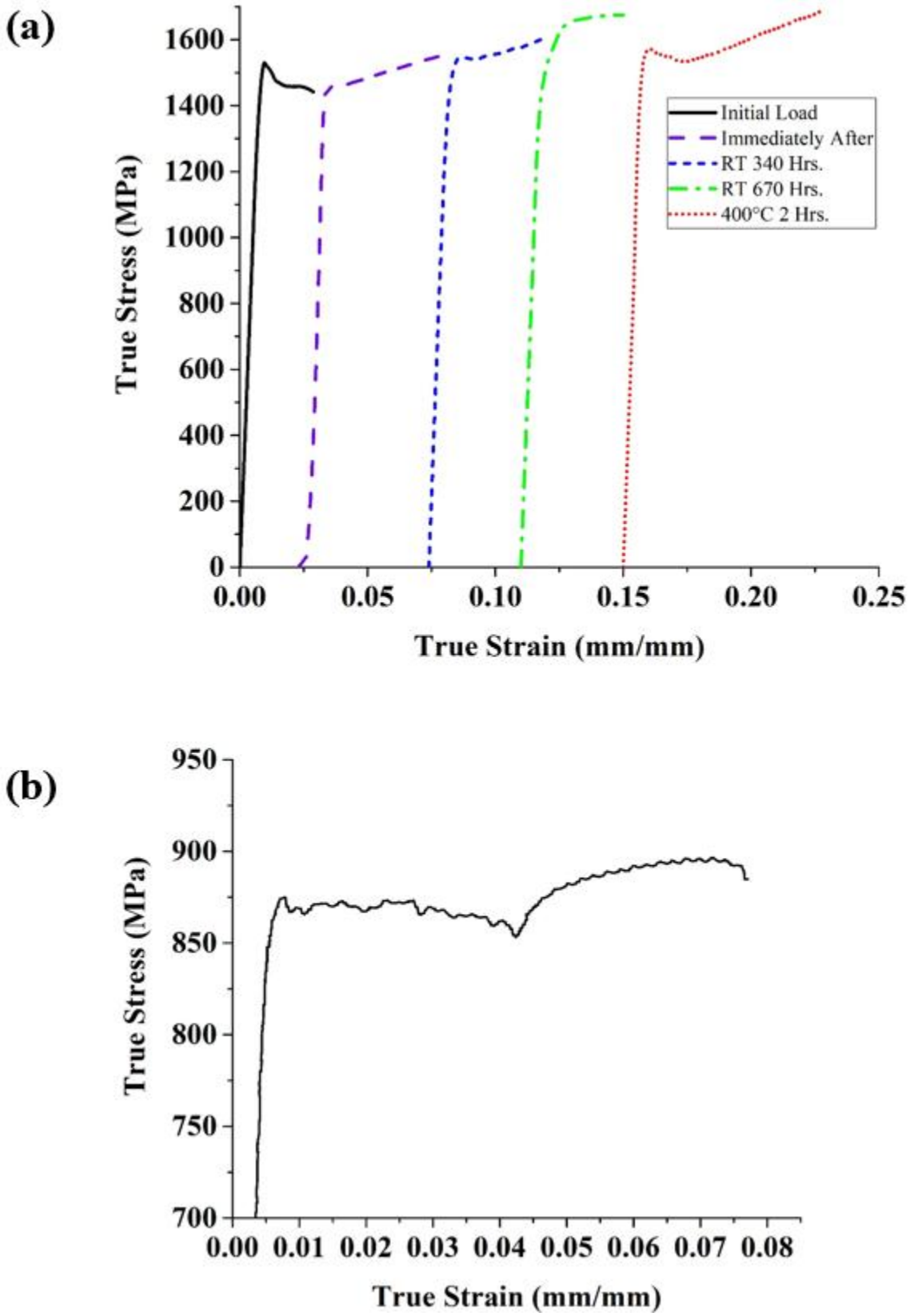
(a)
True Stress (MPa)
True Strain (mm/mm)
Initial Load
Immediately After
RT 340 Hrs.
RT 670 Hrs.
400°C 2 Hrs.
(b)
True Stress (MPa)
True Strain (mm/mm)

Fig. 6

Table 1: Overall, bulk, and solute concentrations. The error was truncated to be consistent with the significant figures given for the mean values.

ECAE Temperature (˚C)	**800°C**			**1000°C**		
Element	**Overall Composition (at.%) (4.8E7 ions)**	**Bulk Composition (at.%) (1.6E6 ions)**	**Zr 8 at.% Isosurface (2.9E5 ions)**	**Overall Composition (at.%) (5.2E7 ions)**	**Bulk Composition (at.%) (3.6E6 ions)**	**Zr 10 at.% Isosurface (2.0E5 ions)**
Fe	89.3±0.0	89.9±0.0	26.7±0.1	89.7±0.0	90.9±0.0	20.0±0.1
Ni	7.9±0.0	8.5±0.0	4.2±0.0	7.2±0.0	7.0±0.0	2.1±0.0
Zr	0.7±0.0	0.3±0.0	27.6±0.1	0.7±0.0	0.5±0.0	29.5±0.1
O	1.0±0.0	0.5±0.0	32.9±0.1	1.0±0.0	0.7±0.0	43.9±0.1
C	0.4±0.0	0.2±0.0	2.7±0.0	0.6±0.0	0.3±0.0	1.1±0.0
N	0.1±0.0	0.1±0.0	3.9±0.0	0.2±0.0	0.2±0.0	2.7±0.0
Cr	0.3±0.0	0.3±0.0	1.3±0.0	0.3±0.0	0.3±0.0	0.4±0.0
Si	0.1±0.0	0.1±0.0	0.3±0.0	0.2±0.0	0.1±0.0	0.2±0.0

Table 2: Stress data from the mechanical tests listed in Figure 3.

ECAE Temperature (˚C)	**800°C**				**1000°C**			
Mechanical Testing Temperature (˚C)	**23°C**		**200°C**		**23°C**		**200°C**	
Strain Rate (s^{-1})	**0.001**	**4000**	**0.001**	**4000**	**0.001**	**4000**	**0.001**	**4000**
Young's Modulus (GPa)	207.7	194.4	165.8	187.7	190.7	194.5	176.2	196.9
High Yield Point (MPa)	1690.9	1895.3	1475.0	1578.1	1435.6	1437.6	1320.0	1239.8
Low Yield Point (MPa)	1684.6	1751.8	**N/A**	1173.9	1431.0	1355.7	**N/A**	933.5